

Article

Thermomechanical Pathways for Accurate Microstructural Control of Ti–7Ag Alloy: Towards a New Generation of Antibacterial Materials for Medical Applications

Julie Deya^{1,2}, Stéphanie Delannoy^{1,2,*}, Philippe Vermaut^{1,3} and Frédéric Prima¹

- ¹ PSL Research University, Chimie ParisTech, CNRS, Institut de Recherche de Chimie Paris (UMR 8247), 75005 Paris, France; julie.deya@chimieparistech.psl.eu (J.D.); philippe.vermaut@chimieparistech.psl.eu (P.V.); frederic.prima@chimieparistech.psl.eu (F.P.)
- ² Biotech Dental SAS, 305 Allées de Craponne, 13300 Salon-de-Provence, France
- ³ Chemistry Department UFR 926, Sorbonne University, 75005 Paris, France
- * Correspondence: stephanie.delannoy@chimieparistech.psl.eu

Abstract: This study delved into exploring microstructural states in a Ti–7Ag alloy to achieve targeted functional and structural properties. Specifically, the focus was on attaining a homogeneously precipitated state and a solid solution, known for their potential to combine functional traits like corrosion resistance and antibacterial activity with structural properties such as mechanical strength. However, obtaining these optimized microstructures presents challenges due to kinetic considerations. A key finding of this study was the crucial role of a pre-deformation stage, prior to heat treatment, to create an even distribution of fine Ti₂Ag precipitates. Moreover, we demonstrated that starting from this precipitated state, a controlled dissolution step could yield a single-phase solid solution with similar grain size. Therefore, a tailored set of thermomechanical treatments was developed to achieve both microstructures, and these metallurgical states were fully characterized combining SEM (BSE imaging and EDS analysis), TEM, and XRD. Associated mechanical properties were also assessed by tensile testing. In addition, the process was proven to be robust enough to overcome potential industrial problems, such as slow cooling rates when water-quenching large ingots. Considering the limited existing documentation on microstructural features in Ti–Ag alloys, this work on this model alloy significantly advanced our current understanding of the broader Ti–Ag alloy system by providing new data and showcasing a tailored approach involving thermomechanical treatments.



Citation: Deya, J.; Delannoy, S.; Vermaut, P.; Prima, F. Thermomechanical Pathways for Accurate Microstructural Control of Ti–7Ag Alloy: Towards a New Generation of Antibacterial Materials for Medical Applications. *Metals* **2024**, *14*, 577. <https://doi.org/10.3390/met14050577>

Academic Editor: Wenlong Xiao

Received: 26 March 2024

Revised: 26 April 2024

Accepted: 3 May 2024

Published: 14 May 2024

Correction Statement: This article has been republished with a minor change. The change does not affect the scientific content of the article and further details are available within the backmatter of the website version of this article.



Copyright: © 2024 by the authors. Licensee MDPI, Basel, Switzerland. This article is an open access article distributed under the terms and conditions of the Creative Commons Attribution (CC BY) license (<https://creativecommons.org/licenses/by/4.0/>).

Keywords: metallurgy; alpha titanium; silver; precipitation; strain; recrystallization; biomaterials

1. Introduction

Ti-based materials are ideal for biomedical applications due to their excellent combination of corrosion resistance, biocompatibility, and mechanical properties. Consequently, the use of standard materials, such as Ti grade 4 and Ti-64 in dental implantology, enables a relatively high success rate of about 90–95% to be reached (survival rates after 5 years of follow-up [1,2]). Among the most frequent issues are peri-implant diseases, with a prevalence ranging from 14.38% to 24.27% [2,3]. This condition impacts the tissues surrounding dental implants due to long-term bacterial colonization of implant components, and manifests in two primary forms: peri-implant mucositis and peri-implantitis. Peri-implant mucositis involves localized inflammation of the tissues with occasional bleeding. This prevalent condition affects approximately 29.48% of subjects and 46.83% of implants [4,5]. On the other hand, peri-implantitis is characterized by inflammation of the peri-implant mucosa along with the loss of surrounding bone. This prevalent condition affects 9.25% of implants and 19.83% of subjects [4,5], and can lead to implant failure in addition to obvious health risks. Consequently, peri-implantitis represents one of the unresolved challenges currently facing contemporary implant dentistry [6]. To prevent these complications, the

development of alloys with antibacterial activity is currently considered. Bactericidal properties can be provided by surface modifications such as antibacterial metal implantation, drug-loaded coatings, or also antimicrobial peptide-coated surfaces (AMPs) [7,8]. However, surface modification approaches may display some drawbacks including coating delamination with respect to implants, coating damage during the screw implantation, or laborious and expensive processes [7]. For these reasons, intrinsic antibacterial alloys can be considered as a promising alternative to produce a new generation of dental implants. This can be achieved by simply alloying a natural antibacterial element with titanium, following a classical and well-controlled metallurgical process. In this work, silver, which is known to have antibacterial properties at the nanoscale [9,10], is chosen as an alloying element.

According to the literature, two possible distinctive mechanisms are involved in Ti–Ag bactericidal activity: a progressive release of silver ions (Ag^+) [11,12] and a direct contact of bacteria with silver-rich precipitates [13–16]. This clearly illustrates that microstructural parameters actually play a key role in the final performance of antibacterial devices. However, the direct link between microstructure and antibacterial effect remains poorly documented. As a fact, in previous studies, the antibacterial activity of metallic materials is mainly comparatively evaluated with respect to alloys chemistry (nominal silver content), regardless of the microstructure, even though silver can be distributed differently depending on the thermomechanical process applied (from pure silver particles remaining after sintering, to solid solution, through silver-rich precipitates [14–17]). Yet, the microstructure remains essential for both the final structural properties of medical devices and for the antibacterial properties themselves, which may be improved when silver-rich precipitates are nano-scaled and densely dispersed [15].

In order to fulfill this need for further and more accurate antibacterial evaluations, this work aimed at providing new insights regarding the microstructural formation on a Ti–7Ag (wt.%) alloy, with respect to thermomechanical pathways. Following this objective, two model microstructures were targeted: (1) a homogeneously precipitated state ($\alpha + \text{Ti}_2\text{Ag}$) as a two-phase microstructure (PS) and (2) a chemically uniform α solid solution as a single-phase microstructure (SS). This metallurgical study, which is mainly designed to improve our knowledge of Ti–Ag alloys and of the microstructural transformations that are taking place in this system, is a first step towards developing innovative antibacterial materials to further offer a new range of dental, and even orthopedic, implants.

2. Materials and Methods

2.1. Ingot Preparation

Ti–7Ag (wt.%) ingot was prepared by arc melting (BÜHLER AM 500, Edmund Bühler GmbH, Bodelshausen, Germany) from raw elements by mixing and melting pure titanium from TIMET (>99.88 at% purity) and silver from STREM CHEMICAL (99.95 at% purity). Silver's boiling point (2162 °C) being fairly close to titanium's melting point (1668 °C), silver was placed inside pieces of titanium to limit its evaporation during arc melting stage. To homogenize the composition, the ingot was melted five times, and then cast into a 1.5 cm wide square bar.

2.2. Thermomechanical Treatments

The bar was homogenized under vacuum during 24 h at 1000 °C and slowly cooled to room temperature (furnace cooling). Resulting homogenized state (HS) was used as an initial state.

During a preliminary study, samples, initially in HS state, were subjected to precipitation heat treatment consisting of 24 h at 600 °C, conducted under secondary vacuum and followed by water quenching. Resulting states were referred as solution treated and aged states (STA) in the manuscript. Pre-deformation step was introduced for some samples through cold-rolling (at room temperature); ratio of thickness reduction (10% or 40%) was then stated in the designation of the sample as in the following example: 10-STA corre-

sponding to a sample cold-rolled up to 10% of thickness reduction and then heat treated at 600 °C.

The second part of the study involved various thermomechanical treatments. First, samples, initially in HS state, were subjected to hot-rolling at 600 °C up to 75% of thickness reduction. An additional step consisting in cold rolling up to a thickness reduction of 40% was then added. Subsequently, specimens were heat treated in molten salt bath with a composition of 32.1 wt.% Li_2CO_3 /33.4 wt.% Na_2CO_3 /34.5 wt.% K_2CO_3 . Various temperatures (650 °C and 750 °C) were tested during 10-min treatments followed by water quenching. Precipitated state, referred as PS, was obtained using this thermomechanical process.

Dissolution treatments under secondary vacuum were then applied on PS state. Various temperatures (800 °C and 850 °C) were tested during 30-min or 1-h treatments followed by water quenching. Solid solution, referred as SS, was obtained using this process.

A final heat treatment, similar to the one described for obtaining STA samples, was conducted from SS state to access a precipitated state with grain boundary precipitation, referred as PS GBP.

2.3. Microstructural Characterization

Specimens were first mechanically polished using #800 and #1200 grit SiC abrasive papers and then electrolytically polished (Lectropol STRUERS, Struers, Ballerup, Denmark), at a voltage of 25 V for 45 s, with a solution containing 66% of methanol, 27% of butanol and 7% of perchloric acid in volume, to obtain mirror-polished surfaces. Back-scattered electrons (BSE) and energy dispersive spectroscopy (EDS) line scan analyses were conducted using a ZEISS Supra 35 FEG-SEM (Carl Zeiss Microscopy GmbH, Jena, Germany) operating at 15 kV equipped with a BRUKER X-Flash 6–60 SSD EDS detector (Bruker AXS GmbH, Karlsruhe, Germany). Electron backscatter diffraction (EBSD) data were acquired on a ZEISS Merlin FE-SEM operating at 15 kV and equipped with a BRUKER e-Flash HR EBSD detector. Resulting patterns were indexed and analyzed with TSL OIM software version 7 using only titanium α phase crystallographic structure ($\text{P6}_3/\text{mmc}$).

Phase identification was carried out using a BRUKER D8 Endeavor X-ray diffractometer equipped with a copper source. Prior to experiments samples were mechanically ground using grit SiC papers up to #4000 and then polished with OP-S non dry 0.25 μm silica suspension (STRUERS) to achieve a mirror-like surface finish.

Additionally, transmission electron microscopy (TEM) observations were performed with a JEOL 2100+ (JEOL Ltd., Tokyo, Japan) operating at 200 kV. Samples were cut in 3 mm diameter discs, mechanically polished with SiC grinding papers down to a thickness of about 150 μm and finally electrolytically thinned using a STRUERS Tenupol twin-jet electropolisher with the previously described methanol-based solution at low temperature (between 253 and 263 K).

The volume fraction of precipitates was calculated using ImageJ software (version 1.53 c). The contrast and luminosity of the BSE images were adjusted to better distinguish the particles from the matrix, after which the area fraction was calculated using the threshold command. The area fraction was then considered to be similar to the volume fraction.

2.4. Mechanical Properties

Uniaxial tensile tests were performed at room temperature and a strain rate of 10^{-3} s^{-1} on a 10 kN INSTRON 5966 tensile machine (Instron, Norwood, MA, USA) equipped with a 10 mm gauge length extensometer. Flat dog-bone tensile specimens were taken along the rolling direction.

3. Results and Discussion

In this work, the nominal composition Ti–7Ag (wt.%) was considered as a model alloy because of its ability to generate both single-phase and two-phase microstructures, depending on the heat treatment applied as shown on the Ti–Ag phase diagram in Figure 1.

The objective of this study was to develop adapted thermomechanical approaches to reach optimized versions of both microstructural states for further material investigation.

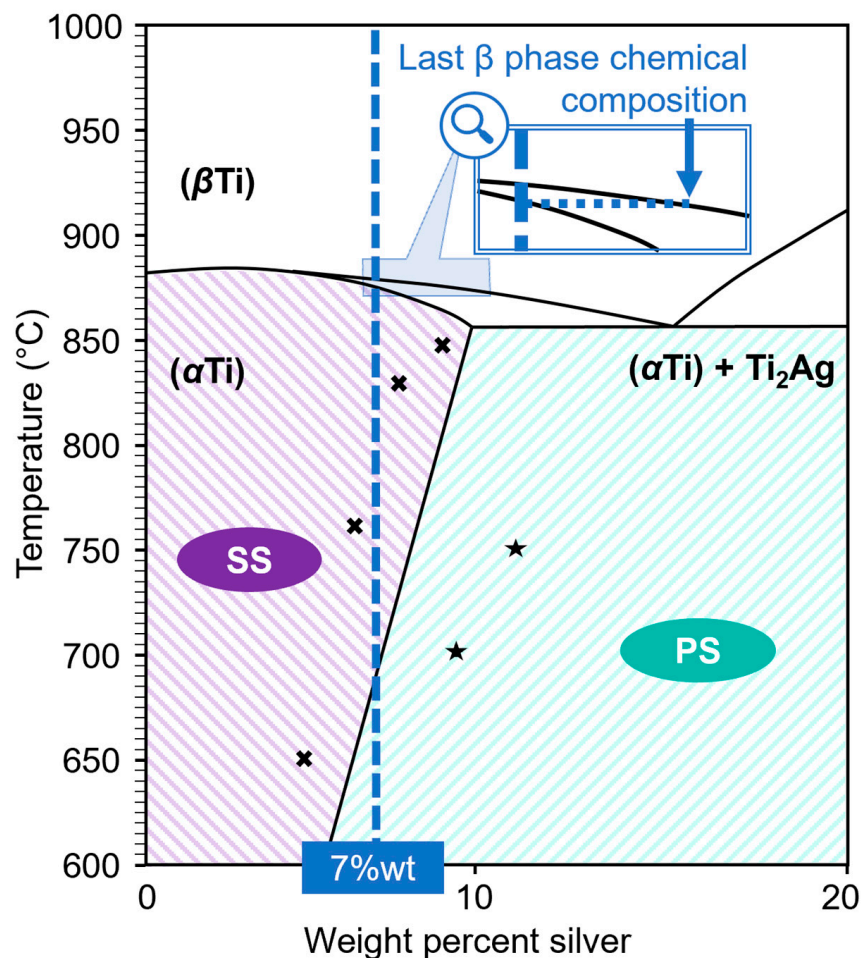


Figure 1. Ti–Ag phase diagram (data from Ref. [18]). Empirical findings are indicated by the following symbols: crosses (data from Ref. [19]) and stars (data from Ref. [20]).

Ti–7Ag alloy was casted and homogenized to obtain a microstructural state hereafter referred as homogenized state (HS). The SEM images and analyses performed on HS are gathered in Figure 2. Very large grains (over 400 μm) are visible in Figure 2a, corresponding to the size of the ex-beta grains formed during the homogenization treatment at 1000 $^{\circ}\text{C}$, and a finer “substructure” can be detected inside these ex-beta grains at higher magnification in Figure 2b. This microstructure corresponds to the formation of large colonies of α plates during the slow cooling process following the thermal treatment at 1000 $^{\circ}\text{C}$. BSE/SEM images clearly display that the chemical homogeneity is not fully ensured in the microstructure and a silver segregation is actually observed as a bright contrast along every α/α interface in colonies. Indeed, BSE imaging, also known as atomic number (Z) contrast imaging, can reveal chemical variations since heavy elements backscatter electrons more strongly than light ones. As a result, in this system, silver-rich areas ($Z = 47$) appear brighter than titanium-rich ones ($Z = 22$). This was confirmed by performing EDS line scan analysis. As shown by the results in Figure 2c, brighter areas corresponding to α/α interfaces turn out to be simultaneously rich in silver and poor in titanium, which eliminates the possibility of a topographical artefact.

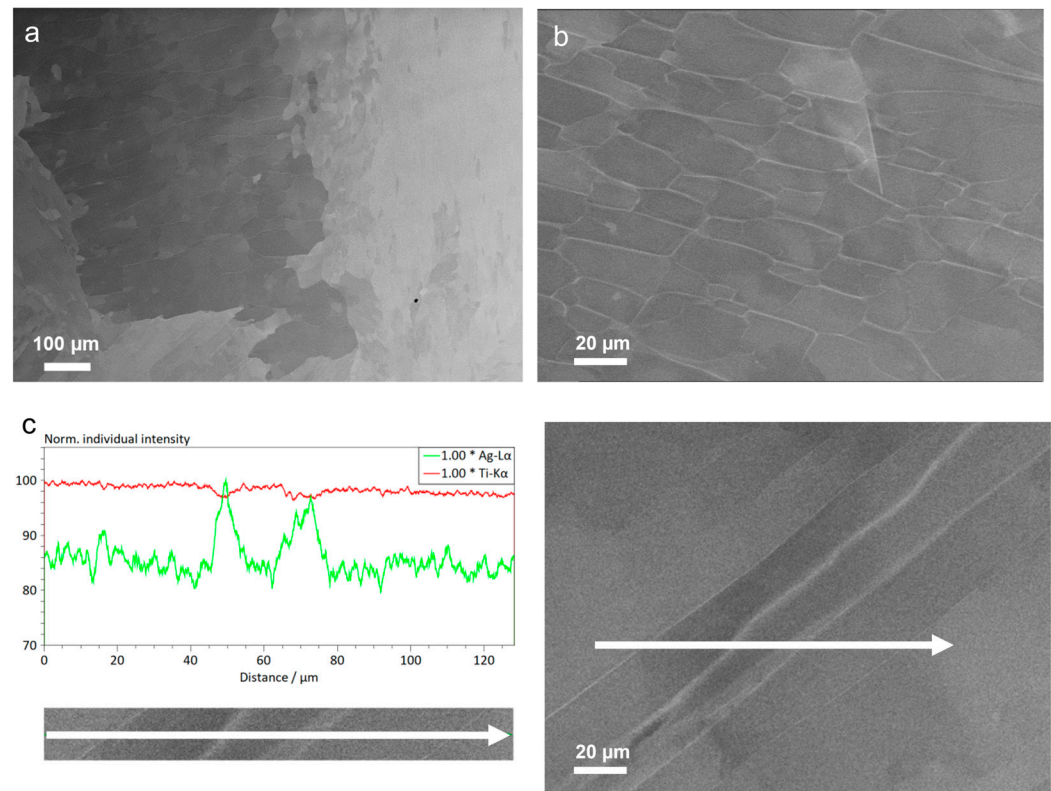


Figure 2. SEM microstructural analysis of Ti-7Ag alloy in initial state (HS). BSE images (a,b) and EDS line scan analysis with corresponding BSE image (c).

There is a question mark over the crossing of the $\alpha + \beta$ two-phase domain (see zoomed inset of the phase diagram in Figure 1), which can result in a fairly high partitioning of silver between the two phases during cooling after the homogenization treatment. The material thus inherits a silver redistribution problem that can occur on an industrial scale when the cooling rate is low. Importantly, this observation is not without consequence for the precipitation stage, as the material evolves strongly out of equilibrium (relative to the phase diagram), the core of the α plates being depleted in silver compared to outer boundaries, which can delay or even eliminate the homogeneous precipitation of Ti_2Ag particles during subsequent heat treatment.

The SEM/BSE observations displayed in Figure 3a consistently show that a 24 h precipitation treatment at 600 °C (STA conditions) fails to properly redistribute the silver within the α platelets, and consequently to produce homogeneous precipitation at the core of these large platelets. After the precipitation treatment at 600 °C, we can observe the presence of a fragmented border located at the interfaces between α plates, indicating that the silver has not been fully redistributed in solid solution in the α phase but has, instead, evolved at the interfaces where it was confined after the high temperature treatment.

There are several possible explanations for this phenomenon: (1) The confinement of Ag atoms, due to a diffusion rate a thousand times slower in α -phase than in β -phase [21,22], and consequently at α/α interfaces, led to subsequent significant Ag depletion in the α phase itself, and the effective chemical composition observed in α -Ti is therefore far from the alloy's nominal composition. (2) The redistribution of silver in the α plates is hampered by the low diffusion coefficient of Ag in α -Ti, which can be explained by the large difference between the respective atomic radii of the Ti and Ag species. (3) The existence of a large barrier to homogeneous nucleation of the Ti_2Ag intermetallic phase (I4/mmm structure).

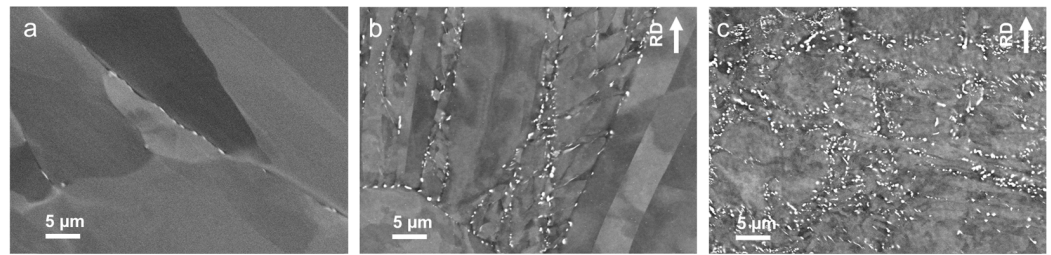


Figure 3. BSE images of Ti7Ag alloy after a precipitation treatment at 600 °C over 24 h (STA) applied on the initial undeformed state (HS) (a), or after a preliminary 10% (b), or 40% (c) thickness reduction by cold-rolling, corresponding respectively to the 10-STA and 40-STA states. Rolling direction is indicated by an arrow.

In this context, a complementary microstructural optimization approach, based on the controlled introduction of a network of dislocations, can be envisaged in order to create diffusion short-circuits in the core of the α platelets. This strategy therefore targets a kinetic action on two levels [23]: to enable better homogenization of Ag atoms in α -Ti and to eventually lower the nucleation barrier associated with the precipitation of homogeneously distributed Ti_2Ag particles in the matrix (which is then enabled by a heterogeneous nucleation mechanism [24]). On this basis, we added a rolling step between the solution treatment and the precipitation treatment. Two rolling rates were implemented by cold rolling on HS: a soft rolling of 10% thickness reduction and an intermediate rolling of 40% before thermal treatment at 600 °C during 24 h (respectively leading to 10-STA and 40-STA states).

The microstructures obtained after the precipitation treatment are shown in Figure 3b,c, and clearly highlight the role of prior deformation in the formation of Ti_2Ag precipitates. The 10-STA microstructure (Figure 3b) is composed of slightly deformed α platelets, and the formation of Ti_2Ag phase particles can be clearly seen both in the vicinity of interfaces where Ag atoms were confined, and at the edges of slip bands formed during cold rolling. It should be noted that the structure did not undergo recovery during heat treatment, as the amount of mechanical energy stored (i.e., the driving force) was probably insufficient to trigger this phenomenon. Figure 3c shows a different microstructure corresponding to the 40-STA state. The microstructure is recovered, as suggested by the disappearance of the large α platelets and due to the greater mechanical driving force introduced by a higher rolling rate. The interesting point lies in the observation of a larger population of Ti_2Ag particles (compared to the 10-STA condition) for an identical precipitation treatment. The spatial distribution of Ti_2Ag precipitates is also different, and seems to be localized around equiaxed zones that are probably cell walls formed during annealing at 600 °C.

These two observations clearly demonstrate the role played by prior deformation on Ti_2Ag precipitation. Dislocations clearly appear to act as effective diffusion short-circuits that initially support the redistribution of Ag atoms into the core of the α -Ti microstructure. They also form preferential nucleation sites since precipitates seem to localize around the high-density zones of the dislocation network (cell walls). Similar results highlighting the link between pre-deformation and precipitation have been previously observed in other titanium alloys [25,26]. Finally, we note the effectiveness of the recovery phenomenon in obtaining more dense and homogeneous precipitation in the α -Ti matrix.

To promote recrystallization of the material, compared to previously described experimental conditions, both the level of deformation and temperature of thermal treatment were increased, since they are critical process parameters. For practical reasons, and in accordance with common industrial practices, the Ti-7Ag alloy in the HS condition was first hot-rolled at 600 °C, with a thickness reduction of 75%, to both activate a dynamic recovery/recrystallization process and a more complete redistribution of Ag atoms into the α -Ti phase. The material was subsequently cold-rolled at room temperature, with a thickness reduction of 40% to get a high quantity of stored mechanical energy for an optimized nucleation rate of Ti_2Ag particles during the final aging treatment.

Then, as far as temperature is concerned, a compromise was sought: it had to be sufficiently high for the recrystallization to happen [27] but still below the α single-phase field so that enough silver-rich precipitates could be obtained. This understanding somehow forces to approach the transition line between the α and ($\alpha + \text{Ti}_2\text{Ag}$) ranges to obtain the expected synergetic effects between recrystallization and precipitation. Two temperatures were therefore tested for the precipitation treatment, 650 °C and 750 °C. For this treatment, the deformed samples were immersed for 10 min in hot molten salt baths and then quenched in water. This type of heating was chosen, and preferred over radiation or convection modes, to ensure uniform and rapid heating and hence promote both recrystallization and high-temperature heterogeneous nucleation of Ti_2Ag . Indeed, faster heating helped to minimize the time for the recovery process to occur, which could detrimentally consume stored mechanical energy. Moreover, if the heating rate is too low, precipitation can prevail and hinder the following recrystallization. In fact, the combination of both phenomena makes the situation very intricate because, on one hand, the deformed microstructure can affect the nature and kinetics of the precipitation and, on the other hand, the presence of precipitates may interfere with recovery and recrystallization processes [28].

Figure 4 shows SEM microstructural observations of as-processed Ti–7Ag specimens, i.e., deformed and subsequently heat treated at 650 °C (Figure 4a–c) or 750 °C (Figure 4d–f). BSE images at different magnifications enable the assessment of the level of precipitation (quantity and distribution of silver-rich precipitates within the matrix) whereas EBSD inverse pole figure (IPF) maps better highlight the degree of recrystallization of the material.

Figure 4a,b reveal that nanometric precipitates (approximately 300 nm in size) are present in the material after treatment at 650 °C, as expected from the phase diagram in Figure 1 (650 °C being in $\alpha + \text{Ti}_2\text{Ag}$ two-phase-field for the studied composition). However, these precipitates are unevenly distributed, leading to regions with a high density of particles neighboring totally depleted zones, which is particularly noticeable at a lower scale. In fact, the microstructure is shown to be strongly heterogeneous. On the EBSD IPF map (Figure 4c), inhomogeneity regarding recrystallization can also be detected. In fact, the microstructure exhibits areas composed of newly formed equiaxed α grains, with uniform colors and relatively flat and smooth grain boundaries, as well as quite large regions, displaying color gradients and fuzzy outlines, decorated by very small grains. These observations indicate that the material is only partially recrystallized after being treated at 650 °C and that deformed and/or recovered areas remain. However, a (0001) texture, so-called “basal” texture, with basal planes aligned parallel to the sheet plane, is observed, which is known to be typical for recrystallized α titanium alloys [29].

In contrast, as can be seen on the EBSD IPF map in Figure 4f, a fully recrystallized microstructure is achieved after deformation and subsequent thermal treatment at 750 °C. Equiaxed fine grains with an average grain size of 15 μm are formed with also a (0001) texture. Interestingly, and despite the fact that 750 °C is theoretically located in the α single-phase field according to the phase diagram, on top of this well-defined grain structure, on BSE images in Figure 4d,e, nanometric spherical silver-rich precipitates of around 100 nm are visible, with a dense, homogeneous distribution throughout the microstructure. This unexpected presence of Ti_2Ag precipitates at 750 °C might be due to discrepancies between theoretical and empirical solubility limits in the phase diagram. Empirical findings (symbols on Figure 1) suggested deviations from theoretical values (solid lines on Figure 1), with some studies reporting solubility limits that differ from theoretical expectations [18]: at 750 °C or 760 °C—which remains close to our study—the solid solubility limit was found to range from 6.5 wt.% [19] to 11.1 wt.% [20]. In addition, such an approach neglects kinetic aspect. As previously stated, during the thermal treatment, a complex combination of events occurs, and the mechanical energy stored in the material in the rolling stage can have a considerable impact on the nature and speed of the precipitation phenomenon. This can lead to a shift of the solvus temperature and explain why silver-rich precipitates are observed after our thermomechanical process. In the end, the heat treatment at 750 °C appears as a good compromise capable of triggering both complete recrystallization of

the microstructure and relatively homogeneous precipitation of the Ti_2Ag phase. This phase appears to be well dispersed in the matrix, with a volume fraction estimated to be approximately 3% using the ImageJ software (version 1.53 c). Therefore, this microstructure will be referred as precipitated state (PS).

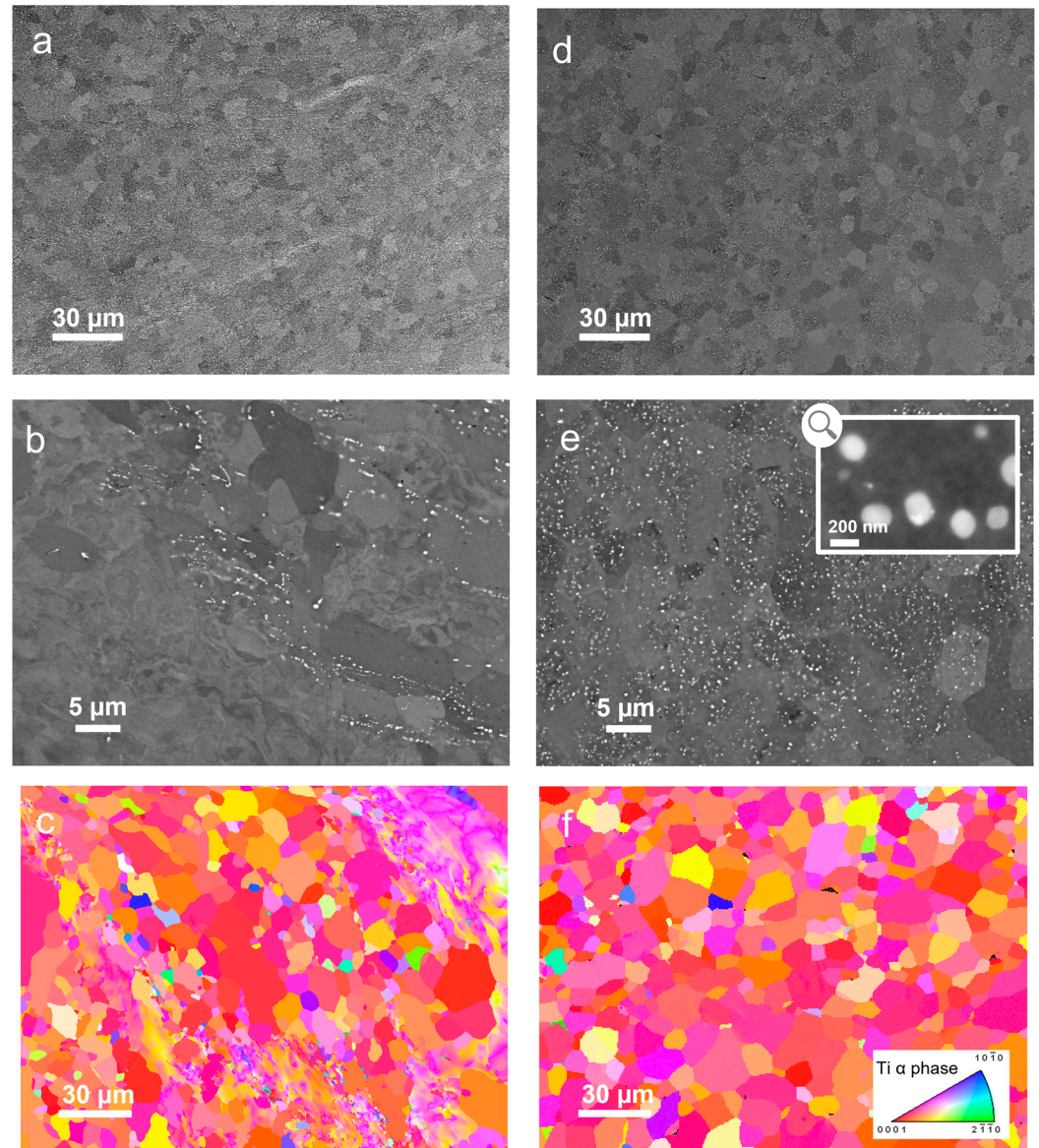


Figure 4. BSE images of Ti7Ag alloy rolled and heat-treated at 650 °C (a,b) or 750 °C (d,e) from homogenized state (HS). Corresponding EBSD IPF maps after treatments at 650 °C (c) or 750 °C (f).

We have seen how complex it is to cool down from the high-temperature β field, due to the inevitable crossing of the two-phase domain ($\alpha + \beta$) for the Ti–7Ag alloy. In order to obtain the most homogeneous single-phase state possible, we therefore used another approach based on a dissolution of the Ti_2Ag precipitates formed during the precipitation treatment at 750 °C. This is the initial state from which we actually have the best chance to obtain a complete redissolution of Ag atoms in the α -Ti matrix with minimized diffusion lengths (the precipitates being nanometric and finely dispersed).

An additional heat treatment stage was therefore introduced to finally reach a homogeneous α -Ti solid solution. Various treatment parameters were tested to achieve the complete dissolution of the silver-rich precipitates while minimizing grain growth, aiming for a grain size comparable to that of the precipitated state.

The dissolution experiments were conducted in a vacuum furnace at higher temperatures (such as 800 °C and 850 °C) when compared to the recrystallization treatment (750 °C), and rapidly cooled by water quenching.

BSE observations made after the various treatment conditions are gathered in Figure 5a–c. As shown in Figure 5a, after 30 min at 800 °C, numerous and still large silver-rich precipitates persist throughout the microstructure, near grain boundaries as well as within the grains. This suggests that the temperature and/or the duration of this treatment were insufficient for substantial dissolution. Subsequently, as can be seen from Figure 5b, after 30 min at 850 °C, only some small and localized bright spots remain, suggesting partial dissolution initiation. It means that increasing the temperature indeed improved the dissolution process, but the duration was still inadequate for achieving complete solid solution due to kinetic reasons.

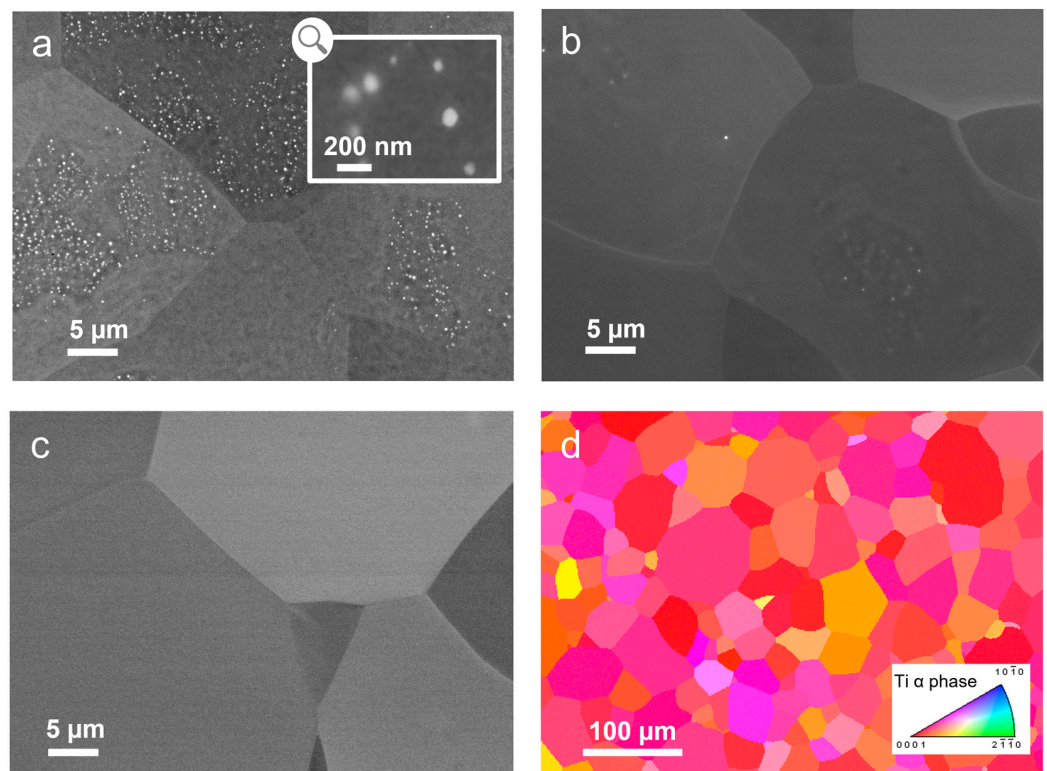


Figure 5. BSE images of Ti-7Al alloy after various heat treatments applied on precipitated state (PS): 800 °C—30 min (a), 850 °C—30 min (b), and 850 °C—1 h (c). Corresponding EBSD IPF map after treatment at 850 °C during 1 h (d).

To progress further, the treatment was extended to 1 h, maintaining the temperature of 850 °C, and, as can be inferred from the BSE image in Figure 5c, a complete dissolution was achieved for these experimental conditions. The microstructure transitioned into the solid solution (SS), as indicated by the absence of visible precipitates in the microstructure. The EBSD IPF map associated to this microstructural state is displayed in Figure 5d. The microstructure is fully indexed with α phase with a basal texture similar to that observed in the recrystallized state (Figure 4f). An increase in the grain size can be noticed, now reaching an average value of 45 μm , which remains acceptable and should not compromise the mechanical properties.

To complete the microstructural investigation and, more particularly, the phase identification, XRD analyses were performed on both previously identified precipitated state (PS) and solid solution (SS). Indeed, especially in the case of the precipitated state, the very low size of the silver-rich precipitates prevented them from being correctly indexed by EBSD.

Both diffractograms are gathered in Figure 6. The purple pattern, at the bottom of Figure 6, corresponds to the solid solution and confirms the presence of only the α phase in the material. As a matter of fact, all the peaks observed match with the titanium hcp structure and no additional contribution is visible. In contrast, the green pattern, at the top of Figure 6, which is associated to the precipitated state, exhibits supplementary peaks. Although they are of low intensity, and some of them can be difficult to discern, being overlapped with α phase signatures, these observed peaks, and particularly those at low angles (2θ around 16° and 36°), seem to indicate the presence of Ti_2Ag phase. This structural identification for the silver-rich precipitates is, therefore, in agreement with the prediction from the binary Ti-Ag phase diagram in Figure 1.

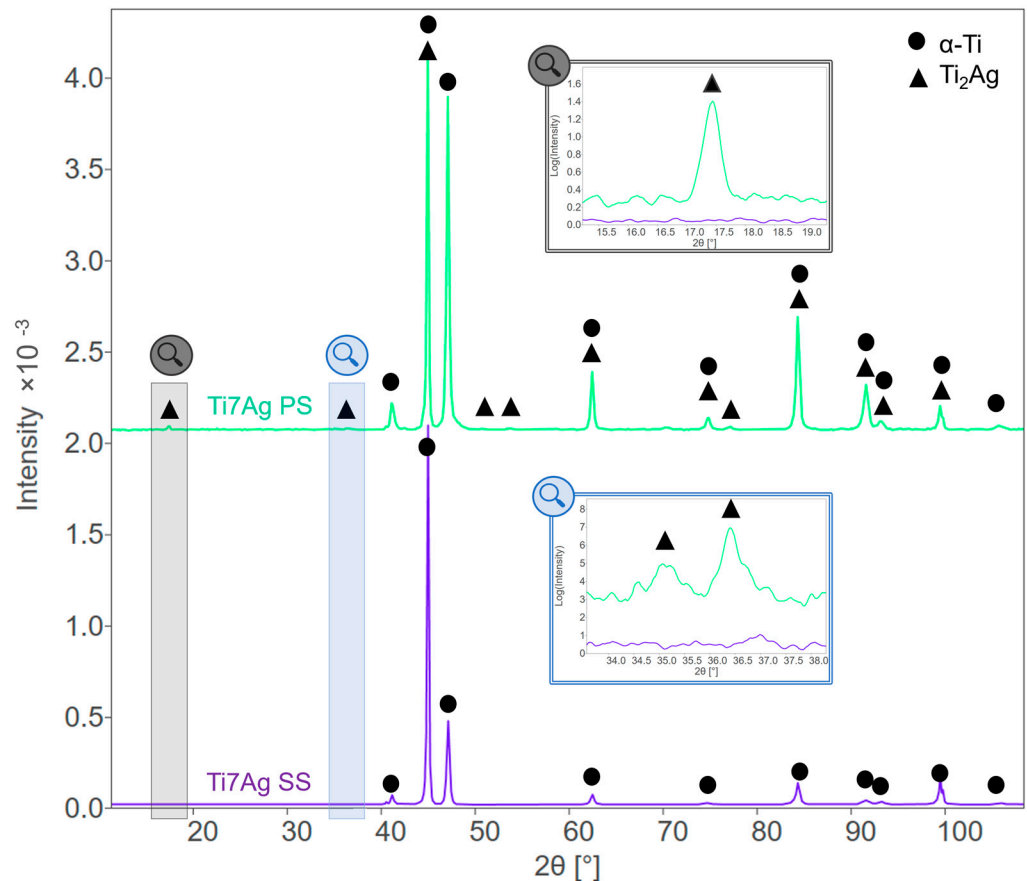


Figure 6. X-ray diffractograms of Ti-7Ag alloy for both precipitated state (PS), in green/top part, and solid solution (SS), in purple/bottom part. Indexation with Ti_2Ag and $\alpha-Ti$ structures (respectively, with triangles and circles). Magnified view of the patterns at low angles is shown in the inset.

For further investigation, TEM observations were performed to confirm their structural identification, as shown in Figure 7. Figure 7a,b display bright field images obtained using different diffraction conditions of the alpha phase and reveal different spherical precipitates around 100 nm diameter, in accordance with those observed in BSE images (Figure 4e). The precipitates were found to be incoherent with the matrix, as only one precipitate can be brought to diffraction conditions at a time (Figure 7a). Therefore, no relationship between the matrix orientation and the precipitate could be identified. Figure 7c–f and Figure 7g–j are the Selected Area Diffraction Patterns (SADPs), recorded, respectively, with the precipitates shown in Figure 7a,b, and their schematic representations. Indexation of these SADPs is consistent with the $MoSi_2$ -type crystal structure of Ti_2Ag belonging to the $I4/mmm$ space group and with lattice parameters $a = 0.2922$ and $c = 1.1998$ nm [30]. SADPs in Figure 7c,e highlight, respectively, the specific c/a ratio and the four-fold symmetry of this crystal structure, in addition to specific Bravais mode extinctions.

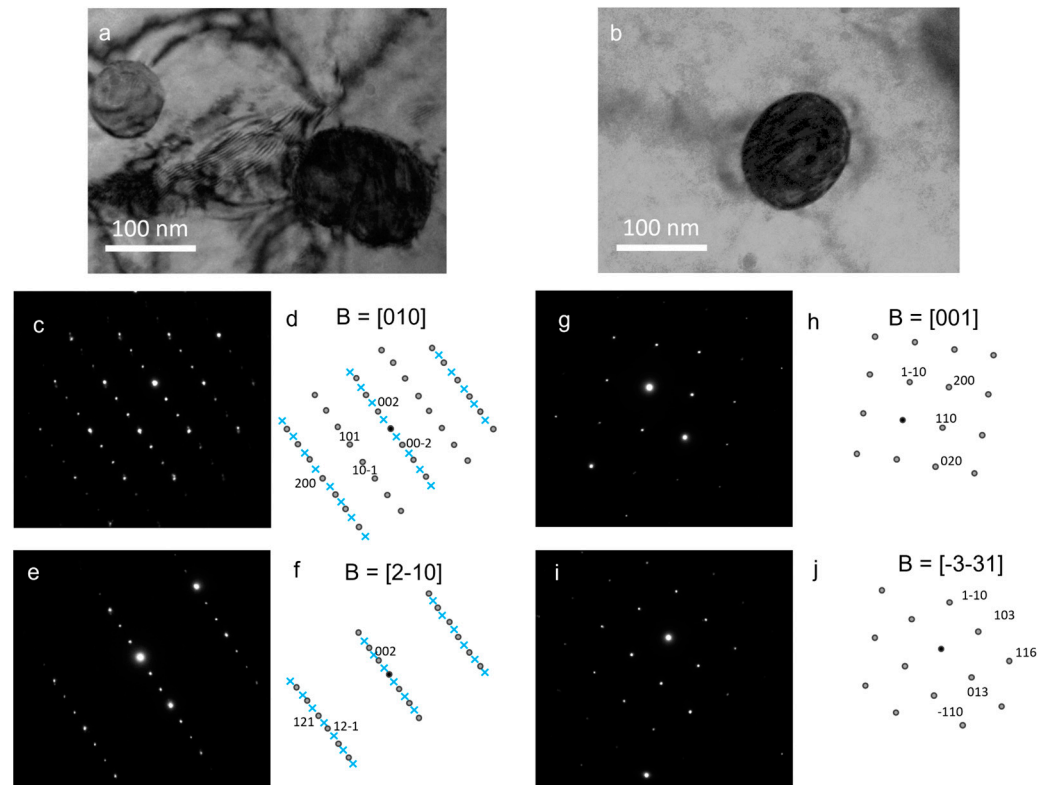


Figure 7. Bright-field TEM images of Ti_2Ag precipitates in $\alpha\text{-Ti}$ matrix (a,b), and corresponding SADPs recorded with the electron beam parallel to the $[010]_{\text{Ti}_2\text{Ag}}$ (c) and $[2-10]_{\text{Ti}_2\text{Ag}}$ (e) direction for the precipitate of image (a) and $[001]_{\text{Ti}_2\text{Ag}}$ (g) and $[-3-31]_{\text{Ti}_2\text{Ag}}$ (i) for the precipitate of image (b). Schematic representations of each SADP (d,h,f,j) annotated with indexation and forbidden reflections (blue \times) consistent with the Ti_2Ag crystal structure.

To sum up, a schematic diagram of the newly developed streamlined process is given in Figure 8, indicating the successive thermomechanical stages used to access the different targeted microstructures. To evaluate further the effect of precipitates size, distribution, and localization, the solid solution was subjected to a 24 h precipitation treatment at 600°C to access a precipitated state with grain boundary precipitation (PS GB).

The mechanical properties of the obtained states in Ti-7Ag were assessed and compared with those of pure and commercial grade 4 titanium. Tensile curves and key values are gathered in Figure 9 and Table 1.

It is observed that solid solution hardening is evident for all Ti-7Ag microstructures compared with pure titanium, which is consistent with the existing literature [31]. More specifically, one can measure the effect generated by the addition of only 7 wt.% of silver to titanium. Though they have comparable grain sizes, Ti-7Ag in solid solution (SS) shows an ultimate tensile strength 50% higher than that of pure titanium, from 270 to 410 MPa, while retaining significant ductility (>20%).

These results also highlight that the distribution and size of precipitates have a crucial impact on the mechanical properties. The material displaying a homogeneous intragranular distribution of nanoscale precipitates (PS) exhibits both higher elongation (34%) and mechanical resistance (540 MPa) compared with the solid solution state (23%, 410 MPa). This enhancement can be attributed to the dispersion strengthening effect imparted by Ti_2Ag precipitates. However, the presence of coarse precipitates concentrated at grain boundaries (PS GB) leads to both reduced elongation (18%) and mechanical resistance (380 MPa). The decrease in strength can be explained by the intergranular precipitation of silver-rich particles which results in a silver depletion in the α -phase matrix and, therefore, in a weakening of the solid solution hardening effect. Additionally, the presence of coarse

and brittle intermetallic phases on grain boundaries, which can already be considered as weak points in the microstructure, negatively impacts the overall ductility.

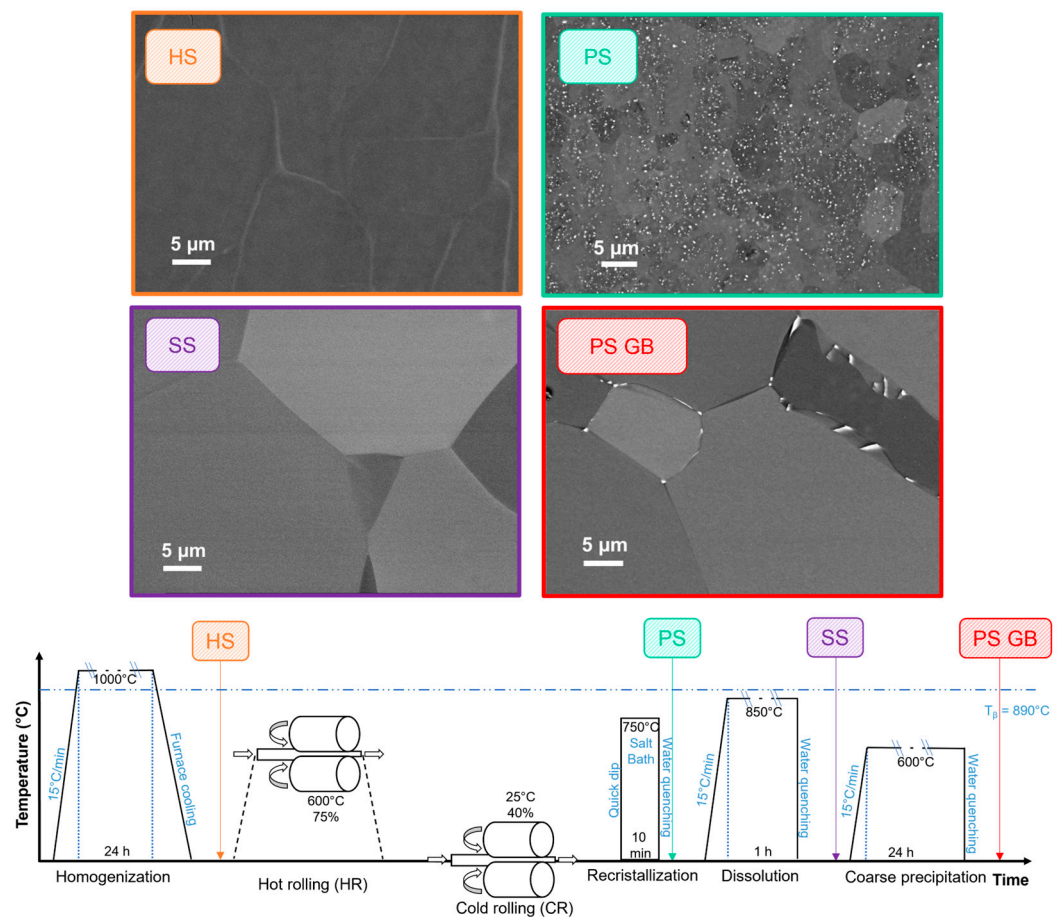


Figure 8. Streamlined process indicating thermomechanical stages used to reach key microstructural states, here referred to as homogenized state (HS), precipitated state (PS), solid solution (SS), and precipitated state on grain boundaries (PS GB), and associated BSE images.

For comparison, Titanium Grade 4 has a minimum ultimate tensile strength of 550 MPa and an elongation at break of 15%, and is commonly used to produce dental implants, especially in cold work conditions. When compared to the present set of experimental results, the precipitated state exhibits the best compromise between ultimate tensile strength (540 MPa) and elongation (34%), largely surpassing the minimum expected value for Titanium Grade 4 in terms of ductility (15%). The considerable elongation observed for this precipitated state suggests that, as in the case of Titanium Grade 4, cold working could be used to further enhance the mechanical resistance of the material.

In summary, the precipitated state in Ti–7Ag demonstrated superior mechanical properties with a balanced combination of high ultimate strength and excellent ductility compared to both the solid solution state and Titanium Grade 4. This notable elongation also opens avenues for potential manufacturing processes, such as cold working, to further improve mechanical characteristics, making it a promising candidate for various applications, including dental implants.

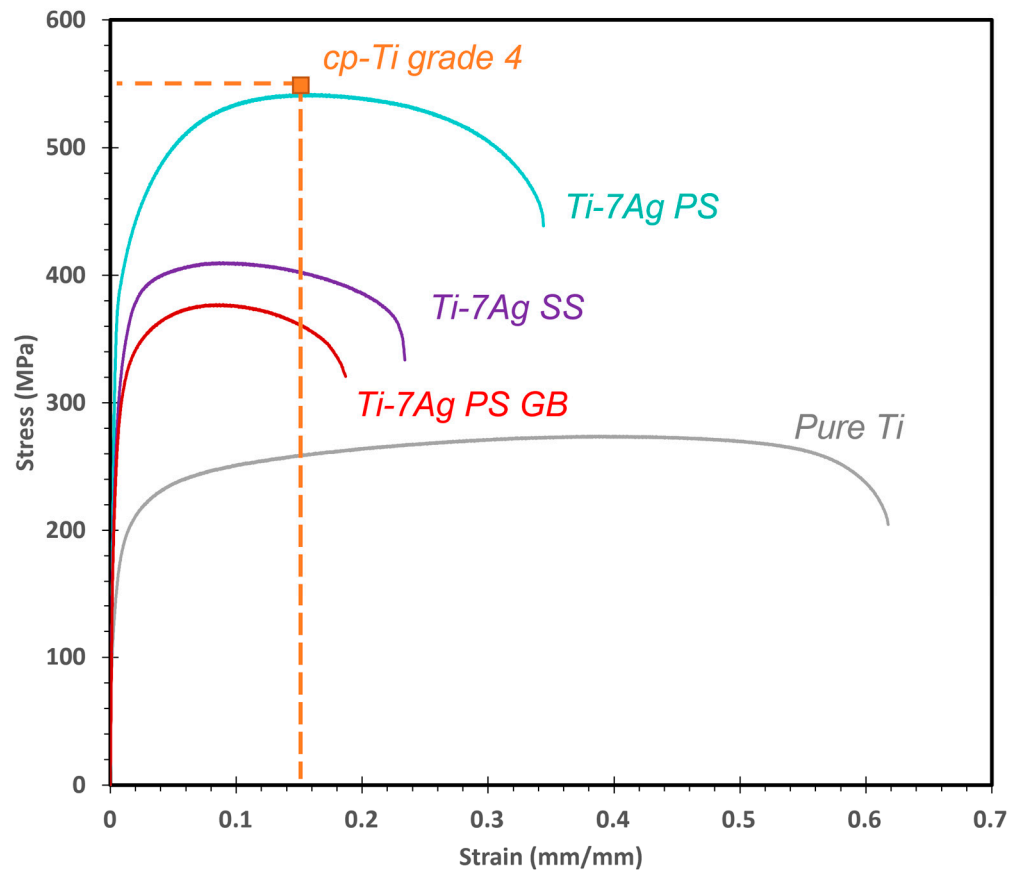


Figure 9. Engineering stress–strain tensile curves of Ti–7Ag (PS, SS, and PS GB conditions), pure titanium with the PS process, and minimum specification for Ti grade 4 according to ASTM F67-13 (data from Ref. [32]).

Table 1. Recapitulative table of mechanical properties of Ti–7Ag alloys (PS, SS and PS GB), pure titanium, and minimum specification for Ti grade 4 according to ASTM F67-13 [32].

Alloys	Ultimate Strength (MPa)	Elongation at Break (%)
Ti–7Ag PS	540	34
Ti–7Ag SS	410	23
Ti–7Ag PS GB	380	18
Pure Ti	270	62
Ti grade 4	550	15

4. Conclusions

This study has shed light on the intricate nature of microstructural control within the Ti–Ag system, primarily due to the disparity in diffusion velocities of Ag between the β and α phases. Notably, the very low diffusion coefficient in the α -Ti phase (around $10^{-16} \text{ cm}^2 \cdot \text{s}^{-1}$) poses challenges in achieving homogeneous precipitation of the Ti_2Ag phase within the α matrix. This limitation hinders the attainment of microstructures that are pivotal for desired functional properties, particularly the antibacterial character, and/or essential structural properties such as mechanical strength.

In light of these challenges, this research underscores the significance of employing indirect thermomechanical treatment pathways. Specifically, introducing sequences of cold or hot deformation proves effective in addressing two crucial aspects: (1) Redistribution of Ag atoms confined to the α/α interfaces post the homogenization treatment at 1000°C .

(2) Significant reduction in the high nucleation barrier of the Ti₂Ag phase, which acts as an impediment to achieving a homogeneous two-phase (α + Ti₂Ag) microstructure.

The proposed final treatment sequence includes intermediate deformation steps that facilitate the coupling of recrystallization and precipitation phenomena, ultimately leading to an optimized final microstructure. The resulting precipitated state demonstrates a promising combination of mechanical properties, boasting an impressive 540 MPa ultimate strength coupled with a 34% elongation.

This achievement paves the way for further complementary studies, particularly in connection with the development of antibacterial implants. The optimized microstructure's mechanical properties encourage further exploration and research, highlighting the potential for the advancement of antibacterial implant technologies.

Author Contributions: Conceptualization, S.D. and F.P.; data curation, J.D.; formal analysis, J.D. and P.V.; funding acquisition, F.P.; investigation, J.D. and P.V.; methodology, J.D.; project administration, S.D. and F.P.; resources, F.P.; supervision, S.D. and F.P.; validation, F.P.; visualization, J.D. and P.V.; writing—original draft, J.D.; writing—review and editing, S.D., P.V., and F.P. All authors have read and agreed to the published version of the manuscript.

Funding: This research was co-funded by ANRT (Association Nationale de la Recherche et de la Technologie) and BIOTECH DENTAL company, CIFRE n° 2020/1556.

Data Availability Statement: All data included in this study are available upon request by contact with the corresponding author.

Acknowledgments: ANRT and BIOTECH DENTAL company are gratefully acknowledged for their financial support on J. Deya grant (CIFRE industrial doctoral fellowship).

Conflicts of Interest: Authors Julie Deya and Stéphanie Delannoy were employed by the company Biotech Dental. The remaining authors declare that the research was conducted in the absence of any commercial or financial relationships that could be construed as a potential conflict of interest.

References

1. Berglundh, T.; Persson, L.; Klinge, B. A Systematic Review of the Incidence of Biological and Technical Complications in Implant Dentistry Reported in Prospective Longitudinal Studies of at Least 5 Years. *J. Clin. Periodontol.* **2002**, *29*, 197–212. [[CrossRef](#)] [[PubMed](#)]
2. Diaz, P.; Gonzalo, E.; Villagra, L.J.G.; Miegimolle, B.; Suarez, M.J. What Is the Prevalence of Peri-Implantitis? A Systematic Review and Meta-Analysis. *BMC Oral Health* **2022**, *22*, 449. [[CrossRef](#)] [[PubMed](#)]
3. Derks, J.; Tomasi, C. Peri-Implant Health and Disease. A Systematic Review of Current Epidemiology. *J. Clin. Periodontol.* **2015**, *42*, S158–S171. [[CrossRef](#)] [[PubMed](#)]
4. Rokaya, D.; Srimaneepong, V.; Wisitrasameewon, W.; Humagain, M.; Thunyakitpisal, P. Peri-Implantitis Update: Risk Indicators, Diagnosis, and Treatment. *Eur. J. Dent.* **2020**, *14*, 672–682. [[CrossRef](#)] [[PubMed](#)]
5. Lee, C.T.; Huang, Y.W.; Zhu, L.; Weltman, R. Prevalences of Peri-Implantitis and Peri-Implant Mucositis: Systematic Review and Meta-Analysis. *J. Dent.* **2017**, *62*, 1–12. [[CrossRef](#)] [[PubMed](#)]
6. Di Gianfilippo, R.; Sirinirund, B.; Rodriguez, M.V.; Chen, Z.; Wang, H.L. Long-Term Prognosis of Peri-Implantitis Treatment: A Systematic Review of Prospective Trials with More than 3 Years of Follow-Up. *Appl. Sci.* **2020**, *10*, 9084. [[CrossRef](#)]
7. Zhang, E.; Zhao, X.; Hu, J.; Wang, R.; Fu, S.; Qin, G. Antibacterial Metals and Alloys for Potential Biomedical Implants. *Bioact. Mater.* **2021**, *6*, 2569–2612. [[CrossRef](#)] [[PubMed](#)]
8. Akshaya, S.; Rowlo, P.K.; Dukle, A.; Nathanael, A.J. Antibacterial Coatings for Titanium Implants: Recent Trends and Future Perspectives. *Antibiotics* **2022**, *11*, 1719. [[CrossRef](#)]
9. Yin, I.X.; Zhang, J.; Zhao, I.S.; Mei, M.L.; Li, Q.; Chu, C.H. The Antibacterial Mechanism of Silver Nanoparticles and Its Application in Dentistry. *Int. J. Nanomed.* **2020**, *15*, 2555–2562. [[CrossRef](#)]
10. Bruna, T.; Maldonado-Bravo, F.; Jara, P.; Caro, N. Silver Nanoparticles and Their Antibacterial Applications. *Int. J. Mol. Sci.* **2021**, *22*, 7202. [[CrossRef](#)]
11. Bao, X.; Maimaitijuma, T.; Yu, B.; Li, X.; Xi, G.; Liu, S.; Cao, Y.; Zhang, T. Ti-Zr-Nb Based BCC Solid Solution Alloy Containing Trace Cu and Ag with Low Modulus and Excellent Antibacterial Properties. *Mater. Today Commun.* **2022**, *31*, 103180. [[CrossRef](#)]
12. Coman, A.N.; Mare, A.; Tanase, C.; Bud, E.; Rusu, A. Silver-Deposited Nanoparticles on the Titanium Nanotubes Surface as a Promising Antibacterial Material into Implants. *Metals* **2021**, *11*, 92. [[CrossRef](#)]
13. Cui, S.; Liu, S.; Nie, J.; Chen, D.; Wu, X.; Qin, G.; Zhang, E. Design and Preparation of a Biomedical Titanium Alloy with Low Elastic Modulus and High Antibacterial Property Based on Ti-Mo-Ag System. *J. Alloys Compd.* **2022**, *908*, 164639. [[CrossRef](#)]

14. Shi, A.; Zhu, C.; Fu, S.; Wang, R.; Qin, G.; Chen, D.; Zhang, E. What Controls the Antibacterial Activity of Ti-Ag Alloy, Ag Ion or Ti2Ag Particles? *Mater. Sci. Eng. C* **2020**, *109*, 110548. [[CrossRef](#)] [[PubMed](#)]
15. Fu, S.; Zhang, Y.; Qin, G.; Zhang, E. Antibacterial Effect of Ti–Ag Alloy Motivated by Ag-Containing Phases. *Mater. Sci. Eng. C* **2021**, *128*, 112266. [[CrossRef](#)] [[PubMed](#)]
16. Song, C.; Chen, Y.; Liu, L.; Lei, H.; Yang, X.; Hu, J.; Li, Q.; Yang, Y.; Li, Y. In Situ Alloying Ti–Ag Antibacterial Biomaterials via Laser Powder Bed Fusion: Microstructure, Mechanical Properties and Bioperformance. *Mater. Today Adv.* **2023**, *20*, 100445. [[CrossRef](#)]
17. Lei, Z.; Zhang, H.; Zhang, E.; You, J.; Ma, X.; Bai, X. Antibacterial Activities and Cell Responses of Ti–Ag Alloys with a Hybrid Micro- to Nanostructured Surface. *J. Biomater. Appl.* **2020**, *34*, 1368–1380. [[CrossRef](#)] [[PubMed](#)]
18. Murray, J.L.; Bhansali, K.J. The Ag–Ti (Silver-Titanium) System. In *Binary Alloy Phase Diagram*; Massalski, T.B., Ed.; American Society for Metals: Metals Park, OH, USA, 1986; Volume 1, p. 77. [[CrossRef](#)]
19. Adenstedt, H.K.; William, R.F. The Tentative Titanium-Silver Binary System. *WADC Tech. Rep.* **1953**, *1*, 53–109. [[CrossRef](#)]
20. Reinbach, R.; Fischmann, D. Einige Ergebnisse von Diffusionsversuchen Im System Titan-Silber. *Int. J. Mater. Res.* **1963**, *54*, 314–316. [[CrossRef](#)]
21. Lee, S.-Y.; Iijima, Y.; Taguchi, O.; Hirano, K. Diffusion of Copper and Silver in β -Titanium. *J. Jpn. Inst. Met.* **1990**, *54*, 502–508. [[CrossRef](#)]
22. Tagushi, O.; Iijima, Y. Diffusion of Copper, Silver and Gold in α -Titanium. *Philos. Mag. A* **2016**, *72*, 1649–1655. [[CrossRef](#)]
23. Larché, F.C. Dislocations in Solids. In *Dislocation in Solids*; Hirth, J.P., Kubin, L., Eds.; Elsevier: New York, NY, USA, 2009; Volume 4, p. iii. [[CrossRef](#)]
24. Sundararaman, M.; Kishore, R.; Mukhopadhyay, P. Some Aspects of the Heterogeneous Precipitation of the Metastable Lambda Dprime Phase in Alloy 625. *Miner. Met. Mater. Soc.* **1994**, 7823–7830. [[CrossRef](#)]
25. Song, Z.Y.; Sun, Q.Y.; Xiao, L.; Liu, L.; Sun, J. Effect of Prestrain and Aging Treatment on Microstructures and Tensile Properties of Ti-10Mo-8V-1Fe-3.5Al Alloy. *Mater. Sci. Eng. A* **2010**, *527*, 691–698. [[CrossRef](#)]
26. Yu, W.; Li, M.Q.; Luo, J. Effect of Deformation Parameters on the Precipitation Mechanism of Secondary α Phase under High Temperature Isothermal Compression of Ti-6Al-4V Alloy. *Mater. Sci. Eng. A* **2010**, *527*, 4210–4217. [[CrossRef](#)]
27. Raabe, D. Recovery and Recrystallization: Phenomena, Physics, Models, Simulation. In *Physical Metallurgy*; Laughlin, D.E., Kazuhiro, H., Eds.; Elsevier: Amsterdam, The Netherlands, 2014; Volume 3, pp. 2291–2399. [[CrossRef](#)]
28. Humphreys, F.J.; Hatherly, M. Recrystallization of Two-Phase Alloys. In *Recrystallization and Related Annealing Phenomena*; Elsevier: Amsterdam, The Netherlands, 2004; pp. 285–319. [[CrossRef](#)]
29. Lütjering, G.; Williams, J.C.; Gysler, A. Microstructure and Mechanical Properties of Titanium Alloys. In *Microstructure and Properties of Materials*; World Scientific: Singapore, 2000; pp. 1–77. [[CrossRef](#)]
30. Schubert, K. Zum Aufbau Der Systeme Titan-Kupfer Und Titan-Silber. *Int. J. Mater. Res.* **1965**, *56*, 197–199. [[CrossRef](#)]
31. Oh, K.T.; Shim, H.M.; Kim, K.N. Properties of Titanium-Silver Alloys for Dental Application. *J. Biomed. Mater. Res. Part B Appl. Biomater.* **2005**, *74*, 649–658. [[CrossRef](#)]
32. *ASTM F67-13*; Standard Specification for Unalloyed Titanium, for Surgical Implant Applications. ASTM International: West Conshohocken, PA, USA, 2017; p. 8. [[CrossRef](#)]

Disclaimer/Publisher’s Note: The statements, opinions and data contained in all publications are solely those of the individual author(s) and contributor(s) and not of MDPI and/or the editor(s). MDPI and/or the editor(s) disclaim responsibility for any injury to people or property resulting from any ideas, methods, instructions or products referred to in the content.